Elastic interaction of protons with stable and exotic light nuclei

M. Y. H. Farag,[1,*] E. H. Esmael,[1] and H. M. Maridi[1,2,†]
[1]*Physics Department, Faculty of Science, Cairo University, Cairo, Egypt*
[2]*Physics Department, Faculty of Applied Science, Taiz University, Taiz, Yemen*
(Received 20 June 2013; published 4 December 2013)

The proton elastic-scattering data on ^{4,6,8}He and ^{6,7,9,11}Li nuclei are analyzed over a wide range of incident energies below 160 MeV/nucleon using the single-folding optical model. The real part of the folding optical potential (OP) is calculated using the M3Y nucleon-nucleon interaction and microscopic densities. The Green's function Monte Carlo density is used for the stable nuclei, whereas the large-scale shell model density is used for the exotic nuclei. The high-energy approximation calculation is used for the volume imaginary OP. The spin-orbit and surface imaginary parts of the OP are constructed from the derivatives of the real and volume imaginary parts of the folded potentials, respectively. The volume integrals of the OPs are studied, and it is found that they show clear dependencies on energy and root-mean-square radii. Hence, it can be considered an important constraint for the choice of the optical potential. A new empirical formula is assumed and successfully applied for the real volume integrals. The obtained results of the differential and the reaction cross sections are in good agreement with the available experimental data. In general, this OP with few and limited fitting parameters, which have systematic behavior with incident energy, successfully describes the proton elastic-scattering data with stable and exotic light nuclei at energies below 160 MeV/nucleon.

DOI: 10.1103/PhysRevC.88.064602 PACS number(s): 25.40.Cm, 25.60.Bx, 21.10.Gv, 24.10.Ht

I. INTRODUCTION

The cross-section data for proton elastic scattering of light nuclei are the main sources of information constraining nuclear structure models of these nuclei and about the mechanisms of interaction. In addition, they are useful tools for testing and analyzing reaction theories. The optical potential models have been developed to study the data for proton elastic scattering of light nuclei. Both phenomenological and microscopic optical models are used with the adjustment of only a few parameters, and cannot give unique values of these parameters. The potentials are quite similar for all nuclei and vary slowly with the incident energy [1].

Light neutron-rich exotic nuclei are characterized by weak binding energies that lead to exotic features such as halos. These nuclei are so short lived that they cannot be used as targets. Instead, direct reactions with a radioactive nuclear beam can be performed in inverse kinematics. In the phenomenological approach, the potential parameters are adjusted by being fit to scattering experimental data. It is successful in a wide region of incident energy. However, it does not include information regarding the structure of interacting nuclei. For the microscopic approach, the effective potential is established theoretically. The microscopic Glauber theory can be used to analyze the scattering data at high energies and to obtain the size and the shape of the nuclear matter distributions.

At relatively low incident energies, the folding model can be considered a successful tool for the analysis of the elastic-scattering data. The basic inputs for a single-folding microscopic optical potential (OP) calculation of the proton-nucleus potential are the nuclear densities of the target and the effective nucleon-nucleon (NN) interaction.

A large amount of experimental data at low and intermediate energies exist for the proton elastic scattering of light nuclei. Most of the experimental data of $p + ^{4,6,8}$He and $p + ^{6,8,9,11}$Li are at energies between 6 and 160 MeV/nucleon, and their references are listed in Table I.

To fit these data, the angular distributions are studied using different phenomenological and microscopic optical potentials that are calculated using a folding model, a Woods-Saxon phenomenological form, or a combination of them. The OP parts that use the single-folding model are renormalized by factors while the phenomenological parameters are optimized to fit the data.

Proton elastic scattering of ^{6,7,9,11}Li at about 60–65 MeV/nucleon was analyzed by Moon *et al.* [34]. It was found that the cross section of $^{11}\mathrm{Li} + p$ is 30% smaller than those of other isotopes. The breakup channel coupling effect is suggested as a possible reason for this depression.

In addition, proton elastic scattering of ^{4,6,8}He and ^{6,9,11}Li at energies 60–75 MeV/nucleon was studied by Korsheninnikov *et al.* [16,17]. They found that the scattering of the ^{6,8}He and ^{6}Li at low energies is very similar and differs essentially from that for ^{4}He, reflecting that ^{6,8}He and ^{6}Li have matter radii greater than that of the α particle. Furthermore, the scattering is not sensitive to a difference in neutron and proton distributions, but it is sensitive to the matter radius of these nuclei, i.e., it feels the density extension in these nuclei in comparison with the α particle.

A consistent analysis is made for the proton elastic-scattering data of ^{4,6,8}He and ^{6,7,9,11}Li at an energy range of 25–75 MeV/nucleon [37]. The real part of the OP is calculated using the isospin-, density-, and momentum-dependent modified Seyler-Blanchard (SBM) NN interaction with different densities, while the imaginary and spin-orbit parts are taken in a Woods-Saxon form. It is found that the real part

*faragyehia@gmail.com
†h.maridi@yahoo.com

TABLE I. Experimental data for proton elastic scattering of helium and lithium isotopes.

Scattering	Incident energy (MeV/nucleon) [Reference]
$p + {}^{4}$He	12.04, 17.45 [2], 31.0 [3], 40 [4], 45, 52.3, 59.6, 64.9 [5], 71.9 [6], 85 [7], and 156 MeV/nucleon [8]
${}^{6}\text{He} + p$	25.1 [9–11], 38.3 [12], 40.9 [13], 41.6 [14,15], and 71 MeV/nucleon [16–20]
${}^{8}\text{He} + p$	15.7 [21], 26.1 [22], 32 [16,17,23], 66 [16,17], and 72 MeV/nucleon [16,17,24]
$p + {}^{6}$Li	6.0, 10.0 [25], 25.9, 29.9, 35, 40.1, 45.4 [26], 49.75 [27], 65 [28], 72 [29], 135 [30], and 155 MeV/nucleon [31]
$p + {}^{7}$Li	6.15, 10.3 [32], 24.4 [33], 49.74 [27], 65 [28], and 155 MeV/nucleon [31]
${}^{9,11}\text{Li} + p$	60 MeV/nucleon [34] for ^{9}Li; 62 [34], 68.4 [35], and 75 MeV/nucleon [36] for ^{11}Li

of the folded potentials needs a reduction factor, indicating the possible effect of a strong breakup channel [37].

Furthermore, ${}^{6,8}\text{He} + p$ elastic scattering data at energies below 100 MeV/nucleon have been calculated using a combination of the folded OP with the M3Y interaction and the OP using the high-energy approximation (HEA) by Lukyanov *et al.* [38,39]. Three types of densities are used: Tanihata, the cluster orbital shell-model approximation (COSMA), and the large-scale shell model (LSSM). The LSSM density of ^{6,8}He is found to be the most preferable one because it leads to the best fit to the data. The surface absorption is rather important for the lowest incident energies [39].

Recently, the Bethe-Brueckner-Hartree-Fock approach was used to calculate the optical potential for analyzing the experimental differential cross section and polarization of the proton scattering of ^{4,6,8}He and ^{6,7,9,11}Li nuclei [40]. The sensitivity of the calculated physical observables on the NN interaction and the density distributions is studied. It is observed that all the NN interactions and the different density distributions reproduce rather well the experimental differential cross sections.

In addition, in Ref. [41], the nucleon elastic-scattering data of ^{6,7}Li at incident energies up to 150 MeV were analyzed using the continuum-discretized coupled-channels method (CDCC) with the Jeukenne, Lejeune, and Mahaux (JLM) interaction [42]. The energy dependence of the normalization factors of the JLM interaction was introduced and determined explicitly from measured neutron total and proton reaction cross sections. Good agreement with CDCC results shows a systematic energy dependence of the determined normalization factors of the JLM interaction, and the importance of the breakup effect of ^{6,7}Li indicates the necessity of using CDCC for systematic analyses of nucleon scattering over a wide range of incident energies.

Furthermore, we studied [43] the proton elastic scattering of exotic light nuclei (^{6,8}He, ^{9,11}Li, and ^{10,11,12}Be) at an energy range of 15–75 MeV/nucleon. The cross-section data were analyzed using the single-folding optical model with the M3Y interaction and phenomenological Gaussian-oscillator (GO) density. The real, imaginary, and spin-orbit parts of the optical potential were constructed only from the folded potentials and their derivatives. These OP parts, their renormalization factors, and their volume integrals were studied. We found that the surface and spin-orbit potentials are important to fit the experimental data. This OP with few and limited fitting parameters, which have a systematic behavior with incident energy, successfully describes the proton elastic-scattering data with exotic nuclei. However, there are few data for the proton scattering of exotic nuclei. In addition, the data do not cover the whole angular range. Furthermore, the data are measured in the energy region of 10–75 MeV/nucleon. A large amount of data, with a larger energy range and a larger angular range, exist for the proton elastic scattering of stable nuclei. Therefore, a comparative and systematic study is essential for the exotic nuclei and their stable isotopes and to understand the effect of increasing the number of neutrons for a given isotope.

In the present work, a microscopic analysis of the available proton elastic-scattering data of the light nuclei, ^{4,6,8}He and ^{6,7,9,11}Li, in the range of 6 to 160 MeV/nucleon is considered. The microscopic OP is calculated in the framework of the single-folding model using the M3Y effective NN interaction, with microscopic density distributions. The real part of the OP is constructed from the single-folded potential, while the volume imaginary part is calculated using the HEA model. The spin-orbit and the surface imaginary terms are calculated from the derivative of the real and the volume imaginary OP, respectively. The values of the renormalization factors of the microscopic OP parts are studied. The fitting parameters are chosen according to the quality of the agreement with available differential and reaction cross sections and restricted by the behavior of the volume integrals with energy. The most important goals of this work are to use a minimal number of fitting parameters in the OP and to obtain the energy dependence of the volume integrals. The formalism is given in Sec. II, while the results and calculations are presented in Sec. III. The conclusions are given in Sec. IV.

II. FORMALISM

A. Folded potential

The nucleon-nucleus potential can be obtained by single folding the density distribution of the nucleus with the nucleon-nucleon effective interaction [44],

$$V_F(r) = \int \rho(\acute{\mathbf{r}}) v_{nn}(s) d\acute{\mathbf{r}}, \tag{1}$$

where $s = |\mathbf{r} - \acute{\mathbf{r}}|$ is the distance between the two nucleons, $\rho(\acute{\mathbf{r}})$ is the density of the nucleus at $\acute{\mathbf{r}}$, and $v_{nn}(s)$ is the effective NN interaction between two nucleons.

The M3Y effective NN interaction is taken into consideration. It was derived by Bertsch *et al.* [45] and obtained from the fitting of the G-matrix element of the Reid-Elliot NN interaction. The parametrized form of the M3Y interaction is

given by [44]

$$v_{nn}(s) = 7999\frac{\exp(-4s)}{4s} - 2134\frac{\exp(-2.5s)}{2.5s} + J_{00}(E)\delta(s), \tag{2}$$

where the term $J_{00}(E)\delta(s)$ is the zero-range pseudopotential with the knock-on strength $J_{00}(E)$, which depends weakly on the bombarding energy E and is given by

$$J_{00}(E) = -276(1 - 0.005E/A)\ \text{MeV fm}^3, \tag{3}$$

where E is the incident energy and A is the mass number of the projectile.

B. High-energy approximation potential

The nucleon-nucleus potential within the HEA was derived in Ref. [46] on the basis of the eikonal phase inherent in the optical limit of the Glauber theory. The HEA OP can be obtained as a folding of the form factors of the nuclear density and the NN-scattering amplitude [38,39,46,47],

$$U_H(r) = V_H(r) + W_H(r) = -\frac{\hbar v}{(2\pi)^2}(\bar{\alpha}_{NN} + i)\bar{\sigma}_{NN} \times \int_0^\infty dq q^2 j_0(qr)\rho(q) f_{NN}(q), \tag{4}$$

where v is the velocity of the nucleon-nucleus relative motion, $\rho(q)$ is the form factor corresponding to the pointlike nucleon density distribution of the nucleus, and $f_{NN}(q)$ is the amplitude of the NN scattering, which depends on the transfer momentum q and can be specified in the form of a Gaussian function [46,47],

$$f_{NN}(q) = \exp(-q^2 r_0^2/4), \tag{5}$$

where $r_0^2 = 0.439$ fm^2 [47] is the range parameter. The quantities $\bar{\sigma}_{NN}$ and $\bar{\alpha}_{NN}$ are the average over isospin total NN cross section and the ratio of the real to imaginary part of the scattering amplitude at zero angle of free nucleons. They both have been parametrized in Refs. [38,47,48] as a function of energy,

$$\bar{\sigma}_{NN} = \frac{N_P N_T \sigma_{nn} + Z_P Z_T \sigma_{pp} + \xi\sigma_{np}}{A_P A_T}, \tag{6}$$

with $\xi = Z_P N_T + N_P Z_T$. The pp and nn cross sections are given (in fm^2) by

$$\sigma_{pp} = \sigma_{nn} = 1.373 - 1.504\beta^{-1} + 0.876\beta^{-2} + 6.867\beta^2, \tag{7}$$

where

$$\beta = \frac{\upsilon}{c} = \sqrt{1 - \left(\frac{m}{\varepsilon_{\text{lab}} + m}\right)^2} \tag{8}$$

is the velocity of the projectile nucleon, $\varepsilon_{\text{lab}} = E/A$ is the incident energy per nucleon (in MeV), and $m = 931.494$ (in MeV) is the unified atomic mass unit. For the np cross section σ_{np}, two expressions are used. If the energy per nucleon $E > 10$ MeV, then

$$\sigma_{np} = -7.067 - 1.818\beta^{-1} + 2.526\beta^{-2} + 11.35\beta. \tag{9}$$

For $E < 10$ MeV,

$$\sigma_{np} = \frac{273}{(1 - 0.0553E)^2 + 0.35E} + \frac{1763}{(1 + 0.334E)^2 + 6.8E}. \tag{10}$$

The average $\bar{\alpha}_{NN}$ is written as

$$\bar{\alpha}_{NN} = \frac{N_P N_T \sigma_{nn}\alpha_{nn} + Z_P Z_T \sigma_{pp}\alpha_{pp} + \xi\sigma_{np}\alpha_{np}}{N_P N_T \sigma_{nn} + Z_P Z_T \sigma_{pp} + \xi\sigma_{np}}, \tag{11}$$

where

$$\alpha_{pp} = \alpha_{nn} = 0.0078 + 0.1762\sqrt{\varepsilon_{\text{lab}}} + 0.014\,36\varepsilon_{\text{lab}} \tag{12}$$

and

$$\alpha_{np} = -0.0301 + 0.2148\sqrt{\varepsilon_{\text{lab}}} - 0.0551\varepsilon_{\text{lab}}. \tag{13}$$

C. Nuclear density distributions

The density distributions of the light nuclei have been determined using several methods. The best method is high-energy proton scattering. Careful analyses of interaction and reaction cross sections using model density distributions have been used to determine experimental density distributions. The density distributions for light nuclei have been obtained through various theoretical models such as the density distribution of Tanihata *et al.* [49], the Green's function method [50], Hartree Fock [51], COSMA [16,17,52,53], LSSM methods [54,55], and others.

Different phenomenological matter density distributions for helium and lithium isotopes have been obtained from the measured proton elastic-scattering cross sections at high incident energies around 700 MeV/nucleon using the Glauber multiple-scattering theory [56–64]. The neutron halo nuclei are assumed to be composed of a core surrounded by a halo of one or more valence neutrons. It is found that the matter distributions of halo nuclei are significantly more extended than those for their cores. The obtained rms radii of the halo nuclei, ^{6}He, ^{8}He, and ^{11}Li, are found to be quite large compared to those of their cores (^{4}He and ^{9}Li). These studies found that the densities that consider the core and halo with different spatial distributions, such as the GO, fit the data well [62–64].

For ^{6,8}He and ^{9,11}Li exotic nuclei, the microscopic LSSM densities are obtained in a complete $4\hbar w$ shell-model space [55] using the Woods-Saxon (WS) single-particle wave function basis with realistic exponential asymptotic behavior.

Furthermore, the microscopic density distributions for $A \leqslant 10$ nuclei are obtained from the quantum Monte Carlo (QMC) calculations of the ground and low-lying excited states of these nuclei using a realistic Hamiltonian containing the Argonne v18 (AV18) two-nucleon potential alone or with Illinois models (IL1-IL5) [65]. The QMC methods include both variational Monte Carlo (VMC) and Green's function Monte Carlo (GFMC) methods [65]. The GFMC calculations using the AV18 + IL2 model are done to obtain the proton and neutron point densities for ^{4,6,8}He [66,67] and ^{6,7,9}Li [65,68].

In this work, the GFMC density is used for the stable nuclei, whereas the LSSM density is used for the exotic

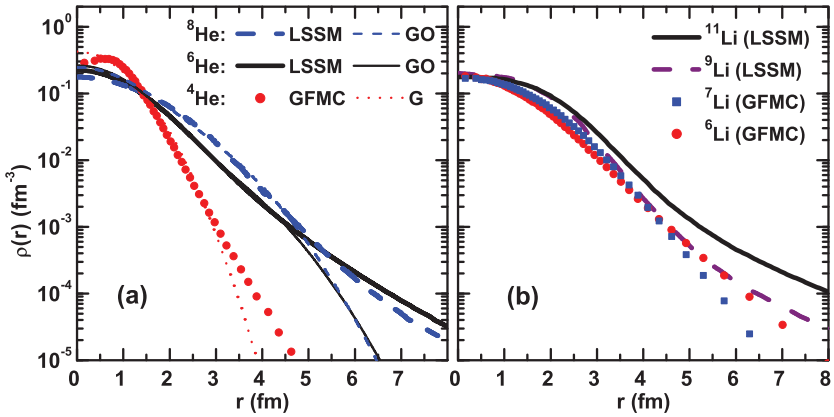

FIG. 1. (Color online) Densities of (a) ^{4,6,8}He and (b) ^{6,7,9,11}Li used in this work.

nuclei. To test the sensitivity to the radial shape of the nuclear matter distribution, the microscopic GFMC density distribution of the ^{4}He nucleus is used for ^{4}He and compared with the phenomenological one-parameter Gaussian density with $R_m = 1.49$ fm [57], whereas the microscopic LSSM density for ^{6,8}He nuclei is compared with phenomenological GO density, where its parameters are given by Tanihata *et al.* [49].

The ^{4,6,8}He and ^{6,7,9,11}Li densities used in this work are presented in Fig. 1. The microscopic distributions of ^{4,6,8}He nuclei (GFMC density for ^{4}He and LSSM density for ^{6,8}He) are plotted in Fig. 1(a) and compared with the phenomenological densities (G for ^{4}He and GO for ^{6,8}He). It is shown that the microscopic densities have tails longer than the phenomenological densities for ^{4,6,8}He. One can see that the ^{4}He density is largest at a small distance ($r < 1.5$ fm), while it falls more rapidly than the ^{6,8}He densities for large r. Figure 1(b) represents the nuclear densities of the lithium isotopes. In general, the distributions of the halo isotopes, ^{6,8}He and ^{11}Li, have extended tails that reflect their halo structure with large radii.

D. Method of calculation

The total optical potential can be generally written as

$$U_{\rm opt}(r) = V_R(r) + iW_I(r) + U_c(r) + U_{\rm SO}(r), \quad (14)$$

where V_R, W_I, and $U_{\rm SO}$ are the real, imaginary, and spin-orbit parts, respectively. $U_c(r)$ is the Coulomb potential of a uniformly charged sphere of radius $1.2A^{1/3}$.

The phenomenological potential parts are taken in the following forms [37,69]:

$$V_R(r) = -V_0 f_0(r), \quad (15)$$

$$W_I(r) = -W_v f_v(r) + 4a_s W_s \frac{d}{dr} f_s(r), \quad (16)$$

$$U_{\rm SO}(r) = 2\lambda_\pi^2 V_{\rm so} \frac{1}{r}\frac{d}{dr} f_{\rm so}(r)\mathbf{L}\cdot\mathbf{S}, \quad (17)$$

where $f_x(r) = [1 + \exp(\frac{r-R_x}{a_x})]^{-1}$, $R_x = r_x A^{1/3}$, and $\lambda_\pi^2 = (\frac{\hbar}{m_\pi c})^2 \approx 2$ fm^2. The subscripts $x = 0, v, s$ and so denote the central real, volume imaginary, surface imaginary, and spin-orbit potentials, respectively. V_0, W_v (W_s), and $V_{\rm so}$ are the strengths of the real, volume (surface) imaginary, and the spin-orbit potentials, respectively.

In the present work, the elastic-scattering cross sections are calculated using the single-folding approach V_F. The phenomenological real and volume imaginary parts of the OP are replaced by the folded potential V_F as seen in Refs. [35,37]. The derivative $(-r\frac{d}{dr}V_F)$ of the folded potential is added as a surface potential [43,70,71]. The spin-orbit part can be obtained microscopically by replacing $f_{\rm so}(r)$ in Eq. (17) by a folding potential V_F [38,43]. The renormalization factors N_R, N_I, $N_{\rm IS}$, and $N_{\rm SO}$ are introduced for the real, volume imaginary, surface imaginary, and spin-orbit microscopic potentials, respectively. They correspond to the strengths V_0, W_v, W_s, and $V_{\rm so}$, respectively. The total microscopic optical potential then can be constructed only from $V_F(r)$ and its derivative and rewritten as

$$U_{\rm opt}(r) = N_R V_F(r) + i\left[N_I V_F(r) - N_{\rm IS} r\frac{d}{dr}V_F(r)\right] - 2\lambda_\pi^2 N_{\rm SO}\frac{1}{r}\frac{d}{dr}V_F(r)\mathbf{L}\cdot\mathbf{S}. \quad (18)$$

In addition, the imaginary part of the OP can be taken with the high-energy approximation model, where $V_F(r)$ is replaced by $W_H(r)$ in the imaginary part of the OP in Eq. (18). Therefore, the OP can be rewritten as

$$U_{\rm opt}(r) = N_R V_F(r) + i\left[N_I W_H(r) - N_{\rm IS} r\frac{d}{dr}W_H(r)\right] - 2\lambda_\pi^2 N_{\rm SO}\frac{1}{r}\frac{d}{dr}V_F(r)\mathbf{L}\cdot\mathbf{S}. \quad (19)$$

The volume integrals of the real and imaginary parts of the OP are denoted by J_R and J_I, respectively. They are defined as [44,69]

$$J_R = -\frac{4\pi}{A}\int [N_R V_F(r)]r^2 dr, \quad (20)$$

$$J_I = -\frac{4\pi}{A}\int [N_I W(r) - N_{\rm IS} r\frac{d}{dr}W(r)]r^2 dr, \quad (21)$$

where $W = W_H, V_F$.

The renormalization factors are determined by a fitting procedure of the cross-sections data which is carried out to achieve minimum χ^2. The χ^2 is given by [44]

$$\chi^2 = \frac{1}{N}\sum_{k=1}^{N}\left[\frac{\sigma_{\rm th}(\theta_k) - \sigma_{\rm ex}(\theta_k)}{\Delta\sigma_{\rm ex}(\theta_k)}\right]^2, \quad (22)$$

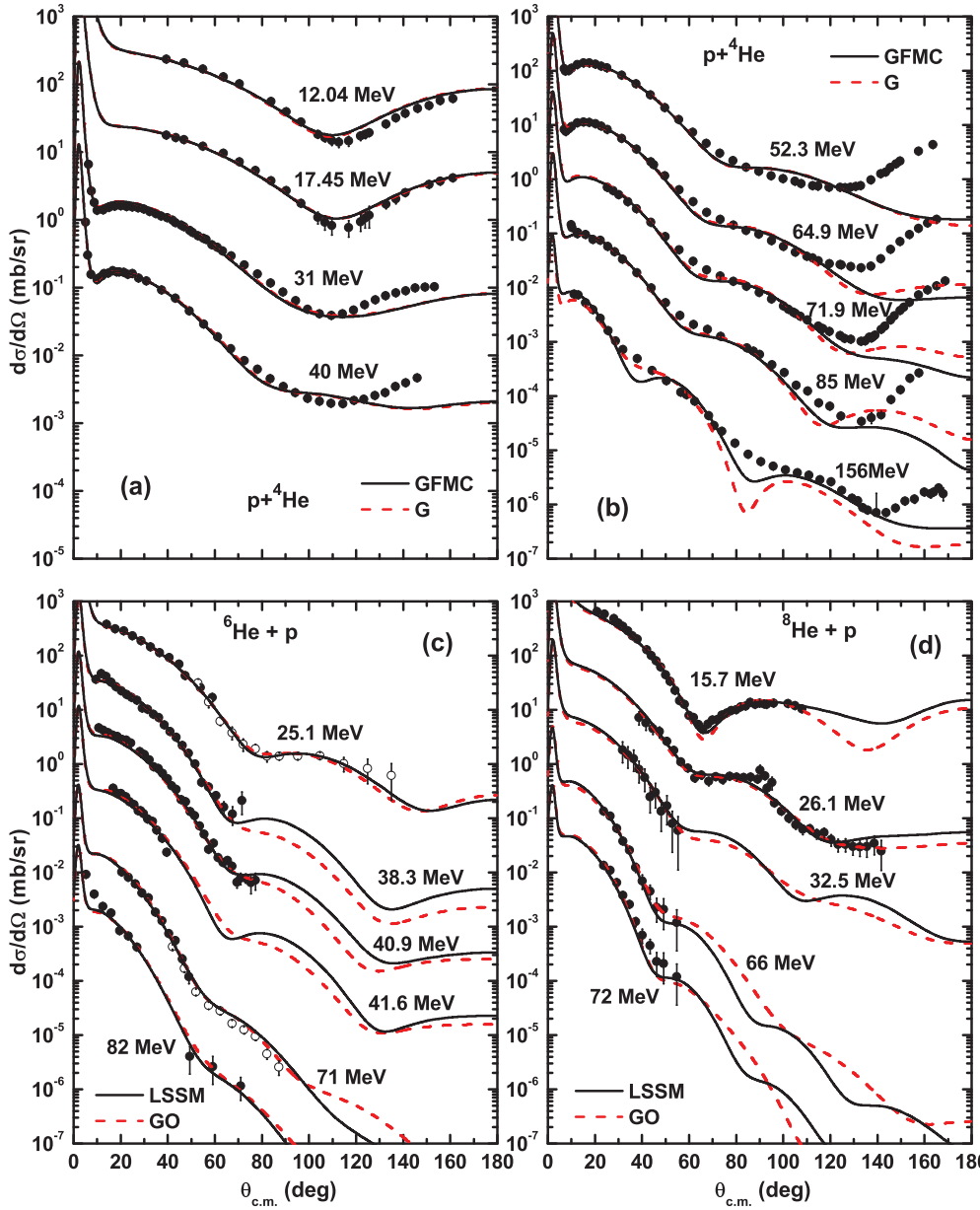

FIG. 2. (Color online) Differential cross sections of proton elastic scattering of helium isotopes (^{4,6,8}He) at different energies (in MeV/nucleon). The solid lines represent the results of calculations with microscopic densities, GFMC for ^{4}He and LSSM for ^{6,8}He. The dashed lines represent the results with the phenomenological densities, G for ^{4}He and GO for ^{6,8}He.

where $\sigma_{\rm th}(\theta_k)$ and $\sigma_{\rm ex}(\theta_k)$ are the theoretical and experimental cross sections at the angle θ_k, respectively, $\Delta\sigma_{\rm ex}(\theta_k)$ is the experimental error, and N is the number of data points.

III. RESULTS AND DISCUSSION

A. Differential cross sections

For Figs. 2 and 3, the incident laboratory energies are indicated in MeV/nucleon. The curves and data points at the top represent true values of differential cross sections, while the others must be multiplied by factors of 10, 100, and so on.

The elastic angular distribution data for the proton elastic scattering of helium isotopes (^{4,6,8}He) at different energies are calculated using the optical potential [Eq. (19)] and shown in Fig. 2. The real part of the OP is calculated using the single folding model with the M3Y interaction, and the imaginary part is calculated with the high-energy approximation model. A comparison between the microscopic and phenomenological densities is presented for each reaction. The renormalization factors of this microscopic OP (N_R, N_I, $N_{\rm IS}$, and $N_{\rm SO}$), the reaction cross sections (σ_R), and the minimum χ^2 of these results are listed in Tables II and III. Figures 2(a) and 2(b) present the results of the proton elastic scattering of the ^{4}He nucleus at different energies calculated using two different densities: the microscopic GFMC and the phenomenological one-parameter Gaussian (G).

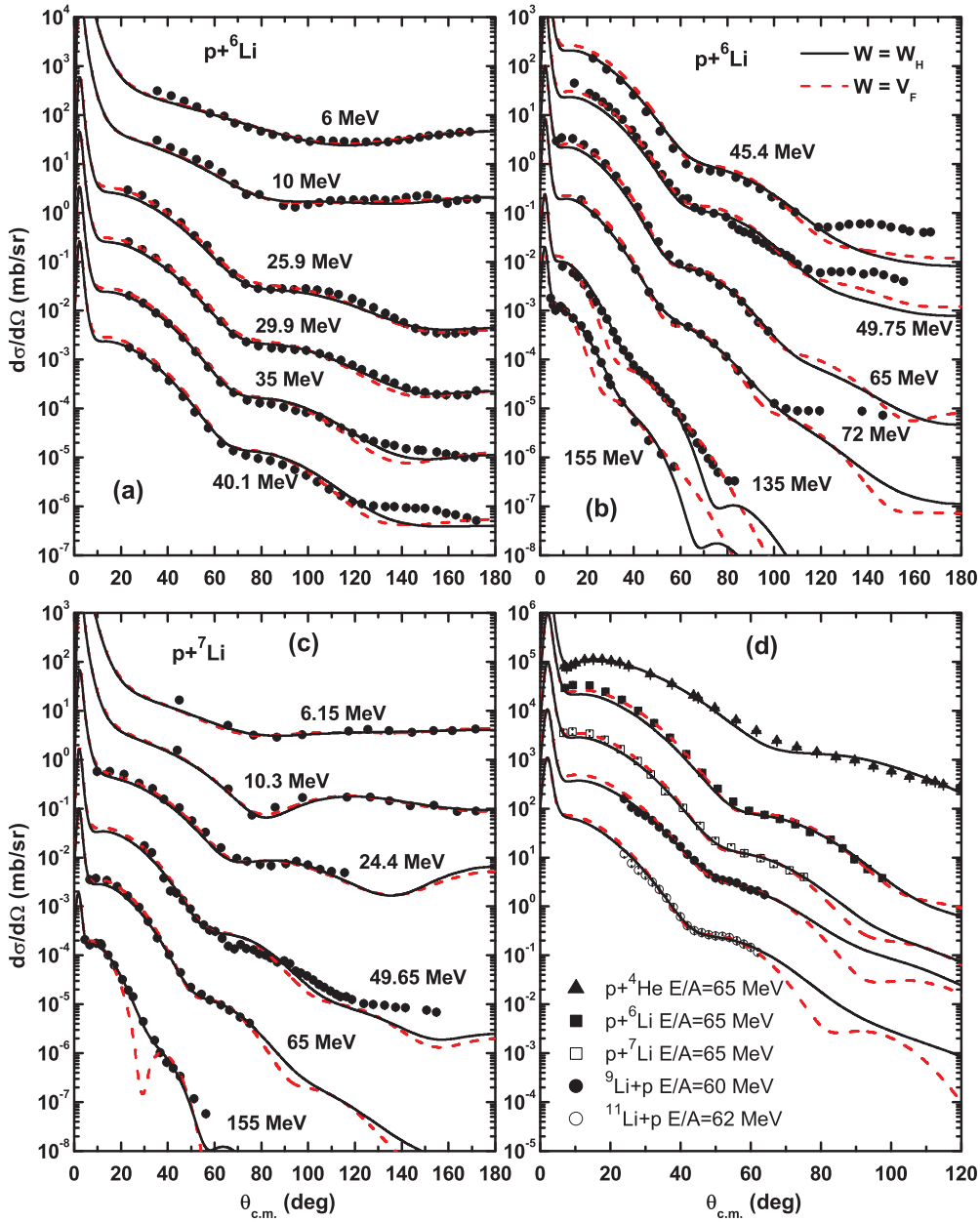

FIG. 3. (Color online) Differential cross sections of proton elastic scattering of lithium isotopes (^{6,7,9,11}Li) at different energies (in MeV/nucleon). The solid and dashed lines represent the results of calculations with HEA [as in Eq. (19)] and M3Y [as in Eq. (18)] folded potentials for the imaginary OP, respectively.

Clearly, from Figs. 2(a) and 2(b) and from the values of χ^2 that are given in Tables II and III, the two densities yield reasonable results for $p + {}^4$He elastic scattering. However, at high energies, the results using the GFMC density are slightly better than those using the G density. At large angles ($\theta > 120^\circ$), the results disagree with the experimental data. This is because we use three parameters only for the fitting procedure, whereas more than ten parameters are used in a fitting with the phenomenological Woods-Saxon potential. Hence, the behavior of the differential cross sections is weakly sensitive to the selection of density. Similar results are mentioned in Refs. [39,57,63,70].

It is found that the N_R values of the real OP using the G density are slightly larger than those using the GFMC density. They decrease slowly if the energy is increased with similar rates. On the other hand, N_I values of the imaginary OP using the two densities are found to be sharply increased with energy up to a definite value and then they slowly change. Furthermore, the values of N_{SO} are in the range of 0.1–0.2 for all the considered energies.

Figures 2(c) and 2(d) present the differential cross sections of ^{6,8}He + p elastic scattering at different energies calculated using the OP [Eq. (19)]. The microscopic LSSM density is used for the two halo nuclei ^{6,8}He and compared with the

TABLE II. Values of the fitting parameters and the calculated reaction cross sections obtained by fitting the experimental cross-section data for the proton elastic scattering of ^{4,6,8}He at different energies using $U_{\rm opt}$ [Eq. (19)] with microscopic densities; GFMC for ^{4}He and LSSM for ^{6,8}He.

Nucleus	E/A (MeV)	N_R	N_I	$N_{\rm IS}$	$N_{\rm so}$	χ^2	σ_R (mb)
^{4}He	12.04	1.35	0.005	0.00	0.10	11.85	27.0
	17.45	1.37	0.01	0.00	0.10	2.88	28.4
	31.0	1.30	0.07	0.00	0.10	30.0	69.8
	40.0	1.29	0.14	0.00	0.10	4.48	88.2
	52.3	1.19	0.36	0.00	0.18	796.0[a]	121.2
	64.9	1.19	0.59	0.00	0.13	443.2[a]	132.5
	71.9	1.22	0.80	0.00	0.16	676.0[a]	142.0
	85.0	1.14	0.90	0.00	0.13	58.0	130.0
	156.0	1.12	1.03	0.00	0.05	38.	90.0
^{6}He	25.1	0.95	0.00	0.15	0.46	0.62	479.4
	38.3	1.0	0.14	0.16	0.34	5.01	406.8
	40.9	1.0	0.15	0.15	0.34	1.82	384.8
	41.6	1.0	0.20	0.16	0.27	1.86	381.1
	71.0	0.93	0.72	0.06	0.00	0.74	277.6
	82.3	0.85	0.80	0.07	0.00	103.71	264.5
^{8}He	15.7	1.00	0.00	0.064	1.12	2.48	578.7
	26.1	1.23	0.00	0.13	0.43	1.70	568.8
	32.5	1.15	0.00	0.15	0.47	0.23	512.7
	66.0	1.05	0.30	0.11	0.20	0.58	310.9
	72.0	1.05	0.40	0.10	0.20	0.93	303.4

[a] χ^2 values are large because the experimental errors are very small, but the visual fit is acceptable.

phenomenological GO density. It is clear that the data fit well with the two densities, LSSM and GO.

From Tables II and III, it is noted that the surface imaginary part of the optical potential is not needed to fit the data of proton elastic scattering on the stable nucleus ^{4}He but it is important to give an agreement with the proton elastic-scattering data of the halo nuclei ^{6,8}He. This is because of the large radii and unusual structures of the halo nuclei. The values obtained for

TABLE III. The same as Table II but with phenomenological densities; G for ^{4}He and GO for ^{6,8}He.

Nucleus	E/A (MeV)	N_R	N_I	$N_{\rm IS}$	$N_{\rm so}$	χ^2	σ_R (mb)
^{4}He	12.04	1.52	0.004	0.00	0.11	9.05	19.61
	17.45	1.50	0.01	0.00	0.12	2.67	25.7
	31.0	1.42	0.077	0.00	0.11	30.6	69.8
	40.0	1.45	0.18	0.00	0.11	4.54	99.0
	52.3	1.34	0.33	0.00	0.14	779.0[a]	108.
	64.9	1.3	0.54	0.00	0.13	437.0[a]	118.
	71.9	1.28	0.79	0.00	0.19	839.0[a]	133.
	85.0	1.25	1.00	0.00	0.16	121.0[a]	143.5
	156.0	1.30	0.97	0.00	0.00	50.53	81.45
^{6}He	25.1	1.0	0.00	0.16	0.47	0.60	457.1
	38.3	1.0	0.00	0.21	0.32	6.10	388.7
	40.9	1.0	0.00	0.20	0.38	1.18	361.1
	41.6	1.0	0.00	0.20	0.25	2.41	355.0
	71.0	0.93	0.74	0.07	0.00	0.82	263.6
	82.3	0.87	0.82	0.07	0.00	113.4	245.3
^{8}He	15.7	0.50	0.00	0.09	1.21	4.21	609.8
	26.1	1.33	0.00	0.14	0.29	1.75	546.7
	32.5	1.0	0.00	0.15	0.46	0.27	476.1
	66.0	1.0	0.88	0.00	0.20	0.40	328.4
	72.0	1.0	0.00	0.23	0.27	1.10	326.9

[a] χ^2 values are large because the experimental errors are very small, but the visual fit is acceptable.

TABLE IV. Renormalization factors and the reaction cross sections, obtained by fitting the experimental cross-section data for the proton elastic scattering of ^{6,7,9,11}Li isotopes using $U_{\rm opt}$ [Eq. (19)] with HEA imaginary OP. GFMC density is used for ^{6,7}Li and LSSM density for ^{9,11}Li.

Nucleus	E/A (MeV)	N_R	N_I	$N_{\rm IS}$	$N_{\rm so}$	χ^2	σ_R (mb)
^{6}Li	6.0	1.48	0.00	0.02	0.38	1.51	365.1
	10.0	1.48	0.00	0.047	0.56	3.59	529.1
	25.9	1.25	0.45	0.00	0.28	7.75	378.0
	29.9	1.17	0.50	0.00	0.30	3.78	352.8
	35.0	1.09	0.53	0.00	0.32	9.31	319.6
	40.1	1.07	0.58	0.00	0.29	28.29	300.4
	45.4	1.04	0.63	0.00	0.17	54.73	283.0
	49.75	1.04	0.64	0.00	0.29	16.44	266.7
	65.0	1.03	0.82	0.00	0.23	4.57	247.7
	72.0	1.02	0.88	0.00	0.13	1056.0[a]	237.8
	135.0	0.80	0.95	0.00	0.15	15.75	154.0
	155.0	0.78	1.14	0.00	0.14	7.81	160.8
^{7}Li	6.15	1.42	0.046	0.00	0.37	1.61	465.0
	10.3	1.51	0.132	0.00	0.46	2.87	584.1
	24.4	1.20	0.30	0.00	0.61	3.82	389.2
	49.74	1.05	0.47	0.00	0.34	14.00	258.3
	65.0	1.02	0.79	0.00	0.17	1.63	274.3
	155.0	1.0	1.0	0.00	0.14	17.68	170.1
^{9}Li	60.0	0.94	0.45	0.00	0.06	1.17	271.9
^{11}Li	62.0	0.94	0.82	0.00	0.00	1.91	441.6

[a] χ^2 values are large because the experimental errors are very small, but the visual fit is acceptable.

$N_{\rm IS}$ for ^{6}He + p are slightly larger than those for ^{8}He + p, because the ^{6}He nucleus has a stronger halo structure than the ^{8}He nucleus. In addition, the surface imaginary OP is found to decrease with an increase of the incident energy. $N_{\rm IS}$ is no longer needed at relatively high energies.

In Fig. 3, the results of the differential cross sections for the proton elastic scattering of lithium isotopes (^{6,7,9,11}Li) at different energies using $U_{\rm opt}$ [Eq. (19)] are presented in comparison with $U_{\rm opt}$ [Eq. (18)]. In this calculation, the imaginary part is calculated with two models: the single-folding M3Y model [$W = V_F$ as in Eq. (18)] and the high-energy approximation model [$W = W_H$ as in Eq. (19)]. The microscopic distributions are used, namely the GFMC density for ^{6,7}Li and the LSSM density for ^{9,11}Li nuclei. The renormalization factors of the microscopic OPs N_R, N_I, $N_{\rm IS}$, $N_{\rm SO}$, the reaction cross sections, and the minimum χ^2 are listed in Tables IV and V.

From Fig. 3 and the values of χ^2 given in Tables V and IV, the results indicate that the two types of imaginary OP reproduce the experimental data well. The M3Y folding imaginary OP gives results with a slightly better fit than the results using the HEA imaginary OP at low energies. However, the HEA imaginary OP gives the best fit at high energies. Furthermore, the value of N_R using the HEA OP is found to be smaller than that using the M3Y folding OP. In addition, the N_I values of the HEA imaginary OP are larger than that of the M3Y folding OP, because the volume integrals of the imaginary OP using $W = W_H$ are smaller than those using $W = V_F$.

In general, from the results of the proton elastic scattering of helium and lithium isotopes, it is noted that N_R values decrease slowly and exponentially with increasing energy. At the same energy, N_R for the halo nuclei is less than that for the stable isotopes. For the imaginary part of the OP, N_I values sharply increase with energy until they reach a maximum value and then slowly change. The value of $N_{\rm IS}$ decreases with increasing incident energy. It has larger values for the halo nuclei. Furthermore, $N_{\rm SO}$ values decrease if the energy increased for most of the considered reactions. More details about the energy dependence of the renormalized OPs and their volume integrals are mentioned in Sec. III C.

B. The reaction cross sections

The total nuclear reaction cross sections (σ_R) tell us about the radii of the scattering nuclei and give information about their structure. In addition, they are considered important constraints for choosing the optical potential parameters. There are available experimental values of the reaction cross sections for reactions of stable nuclei: $p + ^4$He [72,73] and $p + ^{6,7}$Li [72,74] at some energies below 100 MeV/nucleon. In addition, for exotic nuclei, there are available experimental data of the total reaction cross section for ^{6}He + p at 36.2 MeV/nucleon [72,75] and ^{9}Li + p at 34.2 MeV/nucleon [72].

The energy dependence of the reaction cross sections for proton elastic scattering of stable nuclei are presented in Fig. 4. The total reaction cross sections, using both G and GFMC densities, are in agreement with the experimental values and give similar results for $p + ^4$He elastic scattering as shown in Fig. 4(a). They increase with increases in the bombarding energy to about 70 MeV/nucleon. Thereafter, they decrease. The calculated reaction cross sections obtained by using the

TABLE V. The same as Table IV but using $U_{\rm opt}$ [Eq. (18)] with the M3Y single-folded imaginary OP.

Nucleus	E/A (MeV)	N_R	N_I	$N_{\rm IS}$	$N_{\rm so}$	χ^2	σ_R (mb)
^{6}Li	6.0	1.48	0.00	0.06	0.28	1.25	368.9
	10.0	1.54	0.00	0.13	0.56	2.37	547.9
	25.9	1.34	0.54	0.00	0.25	5.09	388.7
	29.9	1.22	0.54	0.00	0.30	8.76	357.5
	35.0	1.12	0.53	0.00	0.34	17.14	324.3
	40.1	1.08	0.55	0.00	0.36	28.91	308.7
	45.4	1.04	0.56	0.00	0.31	59.36	291.6
	49.75	1.04	0.52	0.00	0.43	12.17	266.2
	65.0	1.03	0.50	0.00	0.36	2.35	221.6
	72.0	0.90	0.34	0.07	0.35	1055.0[a]	237.8
	135.0	0.97	0.11	0.23	0.14	12.57	196.4
	155.0	1.20	0.00	0.30	0.05	70.98	185.6
^{7}Li	6.15	1.36	0.128	0.00	0.53	2.06	517.9
	10.3	1.50	0.345	0.00	0.46	2.03	591.1
	24.4	1.10	0.42	0.00	0.66	2.82	391.3
	49.74	1.00	0.47	0.00	0.43	18.0	277.0
	65.0	1.05	0.53	0.00	0.26	1.91	257.7
	155.0	1.10	0.90	0.00	0.16	61.6	196.2
^{9}Li	60.0	1.03	0.39	0.00	0.00	6.83	275.7
^{11}Li	62.0	1.0	0.62	0.00	0.00	4.30	427.7

[a] χ^2 values are large because the experimental errors are very small, but the visual fit is acceptable.

two types of the imaginary OP, HEA OP and the folding M3Y OP, for $p+^{6,7}$Li scattering are shown in comparison with the corresponding experimental data in Figs. 4(b) and 4(c). Clearly, the two types of imaginary parts of OP reproduce the data well and have similar behaviors for the two reactions. In addition, below 10 MeV/nucleon, the expected behavior of σ_R values is that they increase with increasing energy. However, above about 10 MeV/nucleon they decrease with an increase in the bombarding energy.

Figure 5 presents the calculated reaction cross section for proton elastic scattering with helium and lithium isotopes at different energies. The σ_R values obtained for ^{8}He + p elastic scattering are found to be greater than values for ^{6}He + p elastic scattering. They decrease with an increase in bombarding energy, as shown in Fig. 5(a). In addition, these values for ^{6,8}He + p are larger than those for $p+^{4}$He. In general, the calculated σ_R for the halo nuclei scattering (^{6,8}He + p and ^{11}Li + p) are found to be larger than the calculated σ_R for the scattering of their isotopes ($p+^{4}$He and $p+^{6,7}$Li); see Fig. 5. This is related to the rms radius of the scattered nuclei. Furthermore, the results of σ_R for the considered reactions are in agreement with the available experimental data.

In addition, to show the effect of increasing neutron number, Fig. 6 presents the dependence of the reaction cross sections for the proton scattering of helium and lithium isotopes on the mass number and the rms radii. The σ_R are shown in three different energy groups (25, 40, and 71 MeV/nucleon) for helium isotopes in Fig. 6(a). The first group includes $p+^{4}$He at 31 MeV/nucleon, ^{6}He + p at 25.1 MeV/nucleon, and ^{8}He + p at 26.1 MeV/nucleon. The second group contains $p+^{4}$He at 40 MeV/nucleon, ^{6}He + p at 38.3 MeV/nucleon, and ^{8}He + p at 32.5 MeV/nucleon. The third group includes $p+^{4,6,8}$He at about 71 MeV/nucleon. Moreover, the σ_R for proton scattering of lithium isotopes at an energy range of 60–65 MeV/nucleon are shown in one energy group in

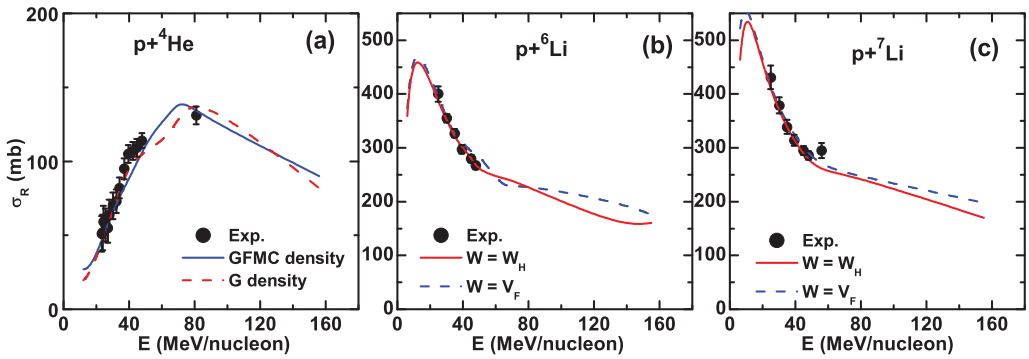

FIG. 4. (Color online) Dependence of the σ_R on the incident energy for the proton elastic scattering of stable isotopes.

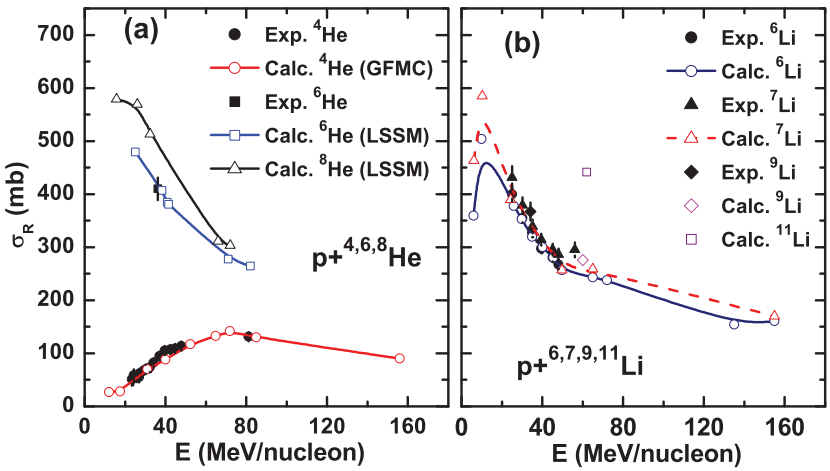

FIG. 5. (Color online) Dependence of the σ_R on the incident energy for the proton elastic scattering of (a) helium and (b) lithium isotopes.

Fig. 6(b). Clearly, the behaviors of the σ_R are similar for the different energy groups for $p + ^{4,6,8}$He elastic scattering. At the same energy, it is found that the values of σ_R that are obtained approximately depend on the matter rms radii of the isotopes presented in Figs. 6(c) and 6(d).

C. The energy and mass dependencies of the volume integrals

1. The energy dependence

Many comparisons are done in this study. The density of the helium isotopes is taken in two forms: phenomenological and microscopic density distributions. The imaginary OP is calculated with two models: M3Y single-folded OP ($W = V_F$) and HEA OP ($W = W_H$).

The volume integrals of the optical potentials for proton elastic scattering with stable nuclei for these comparisons at different energies are plotted in Fig. 7. The volume integrals of the real and imaginary potentials (J_R and J_I) depend on their renormalization factors (N_R and N_I) as seen in Eqs. (20) and (21). The renormalization factors of the OPs are listed in Tables II–V.

It is clear from Fig. 7 and Tables II–V that the real and imaginary volume integrals show a strong dependence on energy. J_R decreases as the energy increases. On the other hand, J_I increases rapidly with energy up to a saturated value. Using both the G and GFMC densities gives similar results for J_R and J_I for $p + ^4$He scattering, as shown in Fig. 7(a). Figures 7(b) and 7(c) show that the volume integrals have similar behaviors for the two reactions, $p + ^{6,7}$Li elastic scattering. Further, the J_I values of the OP with the HEA imaginary potential [Eq. (19)] are found to be slightly larger than those using the folding M3Y potential [Eq. (18)]. This is true for the two reactions.

From these comparisons, the volume integrals of the different types of the OP have similar behaviors for the same reaction. In addition, these different OPs give a good fit for the cross-section experimental data. The question here is in regard to what the most important feature in the OP is: depth, shape, density, interaction, or the volume integral. To get a better understanding, the different types of the OP that are used in this work are plotted in Fig. 8. They are presented with the renormalization factors. The real part of the microscopic OP is calculated using the M3Y single-folding model (V_F) and the imaginary part is obtained within the HEA OP (W_H).

The real and imaginary potentials of ^{4,6,8}He + p at 71 MeV/nucleon, which are calculated at the two different densities: GFMC and G for ^{4}He and LSSM and GO for ^{6,8}He nuclei, are shown in Figs. 8(a) and 8(b). It is shown that the

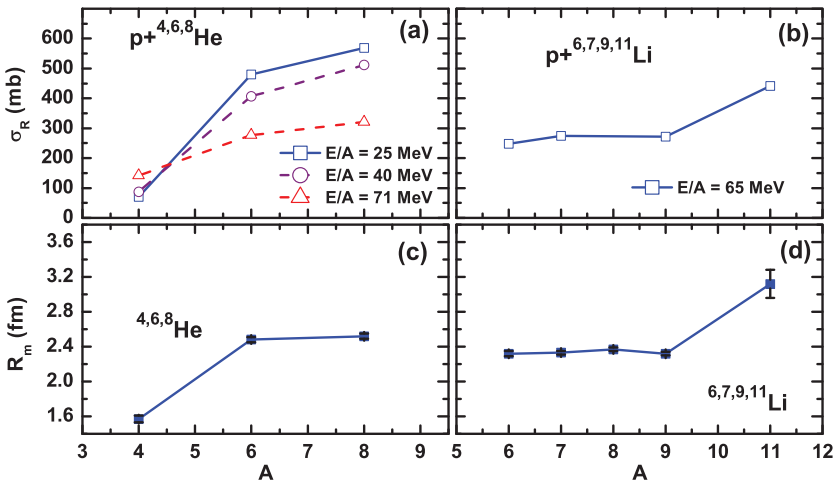

FIG. 6. (Color online) Dependence of σ_R on the mass number for the proton elastic scattering of helium and lithium isotopes using $U_{\rm opt}$ [Eq. (19)]. They are compared with the experimental matter rms radii given in Ref. [76].

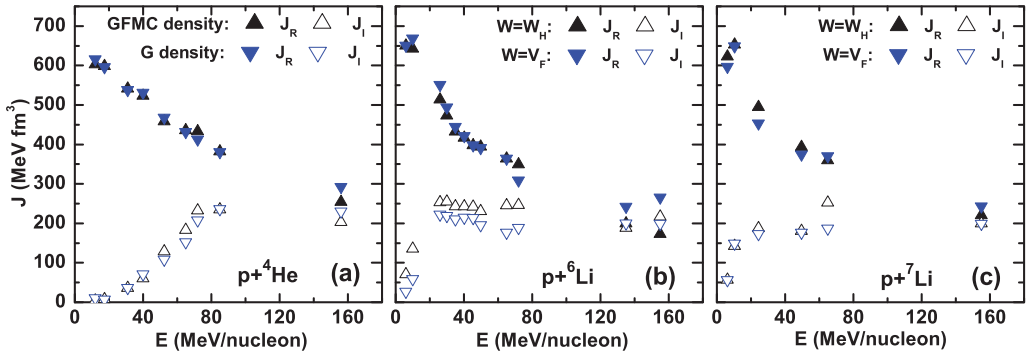

FIG. 7. (Color online) The obtained volume integrals for the proton elastic scattering of stable isotopes [(a) ^{4}He, (b) ^{6}Li, and (c) ^{7}Li].

$p+{}^4$He potentials fall more rapidly at large distances than ^{6,8}He $+ p$ potentials, which have a tail. This is related to the density type of each isotope.

Figures 8(c) and 8(d) present the real and imaginary optical potentials of the proton elastic scattering with lithium isotopes in an energy range of 60–65 MeV/nucleon with the two different forms of the OP as in Eqs. (18) and (19). Here, the imaginary part is obtained within the two forms: the HEA OP (W_H) and the M3Y single-folded OP (V_F).

At small distances, the renormalized real potentials with HEA imaginary OP ($W = W_H$) are shallower than that with folded OP ($W = V_F$) [see Fig. 8(c)]. But this behavior is found to be reversed for the imaginary potentials where the HEA potential has depth larger than the M3Y folded potential for each isotope of lithium [see Fig. 8(d)]. However, the two types of the imaginary OP are close to each other in the surface region.

Clearly, the potentials with different densities or interactions are close to each other at the surface (at $r > 5$ fm), but the

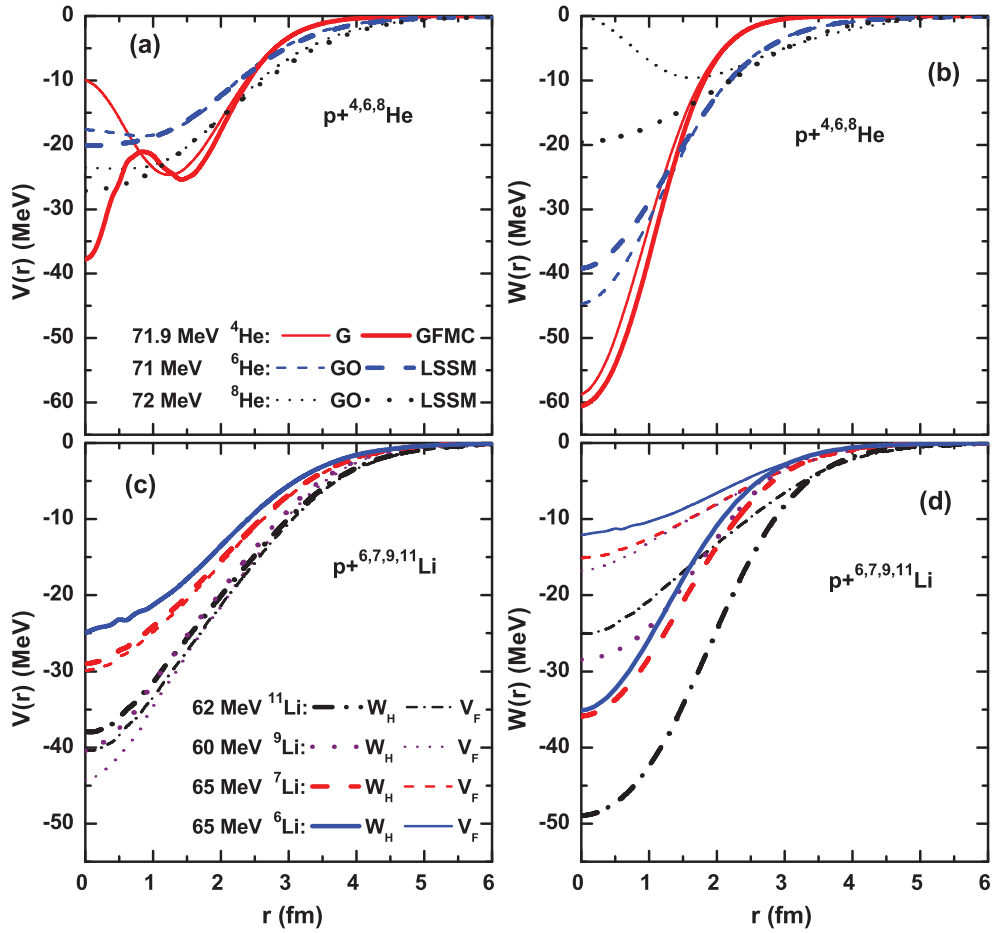

FIG. 8. (Color online) Imaginary optical potentials with many comparisons for proton elastic scattering of helium and lithium isotopes.

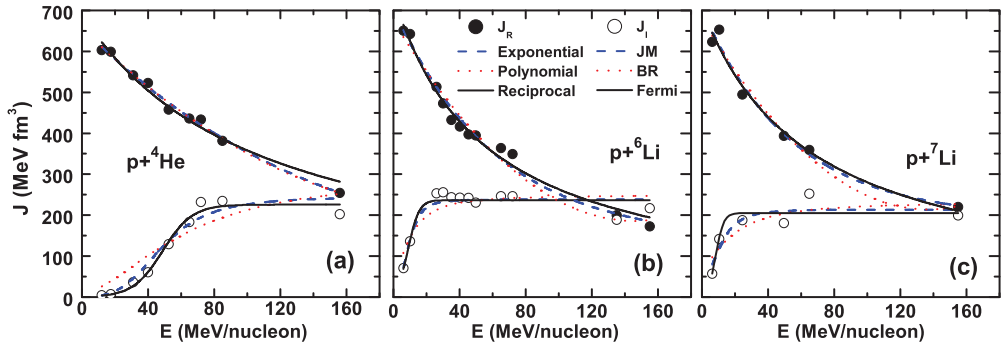

FIG. 9. (Color online) Simulated volume integrals of the OPs [Eq. (19)] as functions of energy for the proton elastic scattering of stable isotopes.

depths of these potentials differ at smaller distances. The fitting procedure, which renormalizes the potential on the whole range, may not give a correct potential at small distances. For the same reaction, the different OPs have different depths and shapes according to the type of density or interaction as mentioned before. Although these OPs differ, at the same time, they give similar fittings to the cross-section data for most of the considered reaction, and their corresponding volume integrals are similar and have closer values as shown in Fig. 7. Hence, the different potentials that give an agreement with the cross-section data should have similar values for their volume integrals. Different energy parametrizations have been proposed for the strengths and the volume integrals of the real and imaginary OP. See, for example, Refs. [77–83].

The energy dependence of the J_R shows a characteristic behavior for all nuclei considered. J_R increases with increasing energy until a maximum is reached at a definite energy (denoted by E_0). Below this energy, a Gaussian parametrization is applied to J_R as [77,84,85]

$$J_R(E) = J_{R0} \exp -(E - E_0)^2/\Delta^2. \quad (23)$$

In the present work, the scattering data at very low energies are not included.

Above E_0, the J_R begin to decrease with energy. Different parametrizations are used for J_R above E_0. The real volume integral can be parametrized in a polynomial form as in Ref. [79],

$$J_R(E) \simeq J_{R0}[1 + \upsilon_1(E - E_F) + \upsilon_2(E - E_F)^2], \quad (24)$$

where J_{R0} is the zero crossing of $J_R(E)$. Another parametrization of the real volume integral can be parametrized by the exponential decay function as [78]

$$J_R(E) = A_0 + A_1 \exp(-\kappa E), \quad (25)$$

with the zero crossing $J_{R0} = A_0 + A_1$.

It is noted that for high energies (about 200 MeV) up to 1000 MeV for proton elastic scattering, the real central potential is known to become repulsive at very high energy and a functional form $J_R(E) \sim \log(E)$ is suitable for the real volume integrals [78,86].

Furthermore, we propose a new empirical formula with two parameters only for the real volume integral. It has a reciprocal form given by

$$J_R(E) = \frac{J_{R0}}{1 + \eta E}, \quad (26)$$

where η is a global fitting parameter. On the other hand, the volume integral J_I of the imaginary part depends strongly on the energy because many reaction channels open at energies around the Coulomb barrier [85,87]. The imaginary part of the potential takes into account the absorption of the flux in the nonelastic channels, so it increases when a new channel is open from $J_I = 0$ below the lowest inelastic channel to a saturation value $J_I = J_{I0}$ observed at relatively high energies [84,87].

The Jeukenne-Mahaux (JM) formula [78,82] is used to express the energy dependence of the volume integrals per nucleon of the imaginary potential as

$$J_I(E) = J_{I0} \frac{(E - E_F)^4}{(E - E_F)^4 + \beta^4}, \quad (27)$$

where E_F is the Fermi energy, which is defined as the energy halfway between the last occupied and the first unoccupied

TABLE VI. Parameters of the parametrizations of the real volume integral J_R for proton elastic scattering of stable isotopes.

Nucleus	Exponential				Polynomial				Reciprocal		
	A_0 (MeV fm^3)	A_1 (MeV fm^3)	κ (MeV^{-1})	χ^2	J_{R0} (MeV fm^3)	υ_1 (MeV^{-1})	υ_2 (MeV^{-2})	χ^2	J_{R0} (MeV fm^3)	η (MeV^{-1})	χ^2
^{4}He	36.6	623.3	0.0068	121.1	691.3	−0.005 85	1.23E-5	119.8	694.4	0.009 37	282.3
^{6}Li	138.8	565.6	0.0161	449.4	709.4	−0.009 77	3.23E-5	751.5	735.3	0.017 19	340.5
^{7}Li	193.8	506.2	0.0183	938.9	776.7	−0.009 65	3.21E-5	1144.2	704.2	0.015 15	733.1

TABLE VII. Parameters of the BR, JM, and Fermi parametrizations of the imaginary volume integral J_I for proton elastic scattering of stable isotopes.

Nucleus	E_F (MeV)	BR parametrization			JM parametrization			Fermi parametrization			
		J_{I0}(MeV fm^3)	Δ(MeV)	χ^2	J_{I0}(MeV fm^3)	β(MeV)	χ^2	J_{I0}(MeV fm^3)	E^*(MeV)	a^*(MeV)	χ^2
^{4}He	−8.922	294.3	67.44	1835.2	244.4	57.52	579.7	225.8	48.82	8.94	204.1
^{6}Li	−5.098	248.5	12.75	918.7	238.3	13.71	432.9	236.7	8.88	3.21	387.8
^{7}Li	−13.616	230.9	23.17	1346.7	213.6	22.53	927.9	205.4	8.39	2.37	813.1

shell of the nucleus and given by [79,80]

$$E_F = -\tfrac{1}{2}[S_p(Z, N) + S_p(Z + 1, N)], \tag{28}$$

where $S_p(Z, N)$ is the proton separation energy for a nucleus with proton number Z and neutron number N. We have used the Audi *et al.* mass table [88] to obtain the values of the separation energies.

Some phenomenological global optical model potentials for the interaction of protons with nuclei as in Refs. [79,80] found that the functional forms from Brown and Rho (BR) [81] gave the best description for all nuclei studied. In the BR parametrization, the energy dependence of the imaginary volume integral can be given in the expression

$$J_I(E) = J_{I0}\frac{(E - E_F)^2}{(E - E_F)^2 + \Delta^2}. \tag{29}$$

In addition, this formula is also used by Refs. [77,84,85,87] for α scattering. In the JM and BR parametrizations, J_{I0} is denoted to the fitted saturation parameter. β and Δ are the rise parameters.

Another Fermi-like parametrization of the imaginary volume integral, first introduced in Ref. [83], reads

$$J_I(E) = J_{I0}\frac{1}{1 + \exp{(E^* - E)/a^*}} \tag{30}$$

with a similar saturation value J_{I0} and the global parameters E^* and a^*. This expression is also used in Refs. [84,85] for α scattering.

The stimulated volume integrals of the OPs for the proton scattering with stable nuclei as a function of energy are shown in Fig. 9. The microscopic OP is calculated using Eq. (19). The fitted parameters of the different parametrizations are listed in Table VI for J_R and in Table VII for J_I.

From this figure and the χ^2 values in Tables VI and VII, it is found that the reciprocal and exponential parametrizations give a fit that is better than the polynomial one for J_R. JM and Fermi parametrizations give a good fit to the J_I values, better than that with the BR formula. But the Fermi formula gives the best fit.

For J_R parametrization, the zero crossing (J_{R0}) and the decay parameters (κ, υ_1, and η) for $p + ^4$He scattering are less than those for the two other scattering reactions ($p + ^{6,7}$Li). In addition, the decay parameters of the J_R for $p + ^{6,7}$Li scattering have closer values as shown in Table VI.

On the other hand, the saturation parameter J_{I0} for different J_I parametrizations has approximately the same value for each of the stable nuclei. It has a large value for ^{4}He and a smaller one at ^{7}Li, whereas the slope parameters Δ, β, and a^* have the largest value for ^{4}He.

2. *The mass dependence*

To study the effect of increasing the neutron number for the same nuclide, Fig. 10 presents the mass number dependence of the volume integrals for the proton elastic scattering with helium and lithium isotopes using the microscopic OP [Eq. (19)]. The renormalization parameters of the OPs are listed in Tables II and IV. The reciprocal parametrization is used for J_R and the JM parametrization for J_I; they have two parameters only. The fitted parameters are listed in Table VIII. For ^{9,11}Li + p scattering at about 60 MeV/nucleon, the J_I is expected to be saturated at this relatively higher energy, because there are

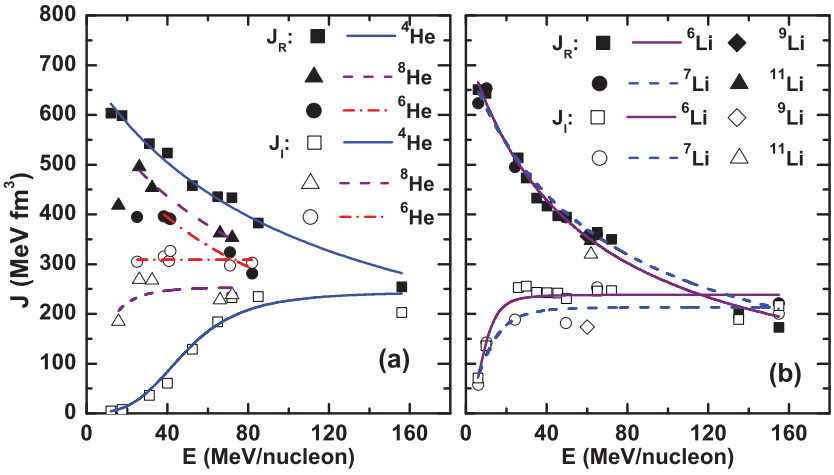

FIG. 10. (Color online) Dependence of the volume integrals on the incident energy for the proton elastic scattering of helium and lithium isotopes. The microscopic OP is calculated by Eq. (19). The symbols represent the calculated volume integrals, and the lines represent the fitted volume integrals using the reciprocal formula for J_R and JM parametrization for J_I.

TABLE VIII. Parameters of the reciprocal and JM parametrizations of the real and imaginary volume integrals for proton elastic scattering of light nuclei.

Nucleus	E_F (MeV)	Reciprocal			JM parametrization		
		J_{R0}	η	χ^2	J_{I0}	β	χ^2
^{4}He	−8.92	694.4	0.009 37	282.3	244.4	57.5	579.7
^{6}He	−16.28	595.3	0.012 78	79.7	308.5		
^{8}He	−19.13	628.9	0.017 26	282.3	253.8	24.2	1044.7
^{6}Li	−5.10	735.3	0.017 19	340.5	238.3	13.7	432.9
^{7}Li	−13.62	704.2	0.015 15	733.1	213.6	22.5	927.9
^{9}Li	−16.79				173.7		
^{11}Li	−19.16				319.9		

no further data for these two scatterings. So, the J_{I0} value is approximately the J_I value at this energy.

Figure 10(a) presents the real and imaginary volume integrals for $p + ^{4,6,8}$He elastic scattering. Clearly, J_R for $p + ^4$He is greater than the two halo nuclei scattering reactions ^{6,8}He $+ p$. Furthermore, the J_R values for ^{8}He $+ p$ elastic scattering are found to be greater than those values for ^{6}He $+ p$ elastic scattering. On the other hand, the J_I values for ^{6}He $+ p$ are the greatest, whereas the J_I values for $p + ^4$He scattering are the smallest. The J_R values for $p + ^{6,7,9,11}$Li lie approximately in the same range of values. However, the J_I of $p + ^6$Li is slightly larger than that of $p + ^7$Li scattering, as shown in Fig. 10(b), whereas the J_I for ^{11}Li $+ p$ scattering is the greatest in the scattering of lithium isotopes. Clearly, the halo nuclei have imaginary volume integrals larger than their stable isotopes. The behavior of J_I then may be related to the rms radius of the scattered nuclei.

In general, the volume integrals of the different OPs have a similar behavior for all the reactions considered in this work. With energy increasing, it is found that J_R increases until a definite value of energy which differs from one isotope to the other. This energy value is found at about 30 MeV/nucleon for ^{6,8}He $+ p$ systems. It may be smaller than 6 MeV/nucleon for stable nuclei scattering, but no scattering data at low energies exist for the exotic case. Therefore, we cannot determine this energy, and more experimental data at low energies are needed. Above this value of energy, J_R decreases exponentially at a slow rate and seems to be saturated at high energies. On the other hand, J_I starts off small at low energies, and then increases rapidly up to a specific energy that depends on the scattering nucleus. This definite energy decreases with increasing rms radius as shown in Fig. 10. More experimental data at relatively high energies, in particular for the exotic nuclei scattering, are needed to determine this energy. Thereafter, J_I values are saturated and seem to be constant. The saturated values are at about 200–300 MeV fm^3. Similar behaviors of the volume integrals are shown in Refs. [78,89–91] for proton elastic scattering with intermediate and heavy nuclei and in Refs. [77,84,85,87] for α-nucleus scattering.

At low energies, the energy dependencies of J_R and J_I are similar to the well-known "threshold anomalies" which are caused by rapid changes in the absorption as the inelastic channels open up near the Coulomb barrier [91].

Furthermore, it is found that the fitted volume integrals using reciprocal parametrization for J_R and JM parametrization for J_I are in good agreement with the calculated volume integrals. In many studies [78–80] for the nucleon elastic scattering of nuclei with an intermediate and heavy mass number ($A \geqslant 24$), the saturation parameter J_{I0} is assumed to be dependent on the mass number. However, J_{I0} depends strongly on the rms radius in the present work, which studies the proton scattering of light nuclei ($A \leqslant 12$).

In addition, Fig. 11 presents the mass dependence of the saturation value of the fitted imaginary volume integrals (J_{I0}). The values of J_{I0} are obtained from the JM parametrization of J_I and are listed in Table VIII. They are compared to the matter and charge rms radii. The experimental matter and charge rms radii of light nuclei are given by Ref. [92] and references therein, namely Refs. [76,93] for matter radii and Refs. [94,95] for charge radii of the helium and lithium isotopes. It is found that the behavior of the J_{I0} value is similar to the behavior of the rms radius for the helium and lithium isotopes. Clearly, the J_{I0} values depend strongly on the charge rms radii of these isotopes as shown in Fig. 11. Generally, most of the experimental data of both the differential and reaction cross sections for the proton scattering with the light nuclei fit well with the microscopic OP used in this work.

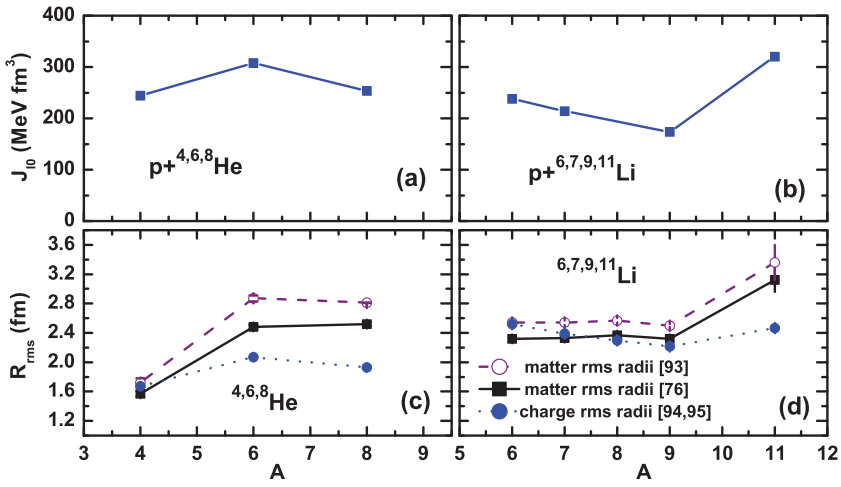

FIG. 11. (Color online) Dependence of the saturation value of the imaginary volume integrals (J_{I0}) on the mass number. J_{I0} values obtained from JM parametrization are listed in Table VIII. They are compared with the experimental matter and charge rms radii which are given by Ref. [92] and references therein.

There are some properties for this OP that are better than the phenomenological and semimicroscopic OPs that were used in the previous works for the same considered reactions, see, for example, Refs. [34,37,70,96,97]. First, the OP parts are constructed only from the folded potential and its derivative. Second, it has only a few and limited fitting parameters, so it is not necessary to introduce a large number of arbitrary fitting parameters used in the phenomenological and semimicroscopic OPs. Third, the fitting parameters showed systematic behaviors with respect to the incident energy and the rms radius. Fourth, this microscopic OP is related to the matter density, whereas the phenomenological potential is a generalized description and does not include any information regarding the structure of interacting nuclei. Finally, the volume integrals of this microscopic OP depend strongly on the rms radius so it can be used to give information regarding structure.

More experimental data for the exotic nuclei with a whole angular range and more studies for scattering data of different light nuclei that were not considered in this work are needed to present a complete picture.

IV. CONCLUSIONS

The optical potentials and cross sections for the proton elastic scattering of some light stable and exotic nuclei, namely ^{4,6,8}He and ^{6,7,9,11}Li, were calculated at energies below 160 MeV/nucleon. The real and spin-orbit parts of the optical potentials were constructed from the single-folding potentials and their derivatives using the M3Y effective nucleon-nucleon interaction and the microscopic densities. The GFMC density was used for stable nuclei, whereas the LSSM density was used for exotic nuclei. The volume imaginary part of the OP was obtained from the HEA and compared with that obtained with the single-folded M3Y potential. The surface imaginary OP was added as the derivative of the volume imaginary OP. The renormalization factors N_R, N_I, $N_{\rm IS}$, and $N_{\rm so}$ for the real, volume imaginary, surface imaginary, spin-orbit microscopic potentials were introduced, respectively. These factors and the volume integrals of the OP parts were studied.

Many comparisons were taken into consideration for different types of densities and interactions. A comparison of the phenomenological and microscopic density distributions were performed for the helium isotopes and the sensitivity of the cross sections to these densities was tested. In addition, a comparison for the imaginary OP with the M3Y single-folded and HEA models was taken in the study of $p+^{6,7,9,11}$Li elastic scattering.

The calculated reaction and differential cross sections are in good agreement with the corresponding experimental data for most of the considered data. This is true for using the different types of the OP.

The σ_R decreases with increasing projectile incident energy for most of the reactions, except for the σ_R for $p+^4$He elastic scattering, which increases with energy. At the same energy, the calculated values of σ_R are clearly dependent on the matter rms radii of the scattering nucleus.

Using the microscopic densities obtained from experimental data produced results as good as those of the phenomenological ones. The imaginary OP using the M3Y folding model gives results with a slightly better fit than results using the HEA model at low energies, but the HEA imaginary OP gives the best fit at high energies. In general, the two types of the imaginary OP give a good fit to the data. The results show that the volume imaginary part is more important than the surface part to fit the experimental data of the stable nuclei scattering. However, the surface part is significant to fit the data of exotic nuclei. This is related to the unusual structures of these nuclei. In addition, the surface imaginary OP is not needed at relatively high energies (>70 MeV/nucleon).

The volume integrals of the different OPs have a similar behavior regarding energy for all the reactions considered in this work. J_R increases with energy to a definite value of energy. Thereafter, with an increase in the incident energy, the J_R values decrease slowly and exponentially. On the other hand, the J_I values increase rapidly up to a definite value of energy that depends on the rms radius of the scattering nucleus. After this value of energy, the J_I values are saturated or may be decreasing linearly with a very slow rate. The dependence of the imaginary volume integrals on the increasing of the neutron number shows a strong dependence between J_I values and the rms radius of the scattered isotope at the same incident energy. The J_I values increase with an increase in the rms radius of the isotope and vice versa.

In the fitting procedure, the renormalized OPs and their depths, which give an agreement with the cross-section data, may vary depending on the shape, density, or interaction type used. However, at the same time, they give similar volume integrals. Hence, the volume integral that gives the fitting with data is more important than the other features of the OP, and it can be considered an important constraint for the choice of the optical potential.

For the energy dependence of real volume integrals, different parametrizations such as exponential and polynomial forms with three parameters are employed. In addition, we suppose and apply a new parametrization (reciprocal form) with two parameters for J_R. On the other hand, the energy dependence of the imaginary volume integral is given by the conventional BR, the JM, and Fermi-type parametrizations. The reciprocal formula for J_R and JM parametrization for J_I are preferred because they consist of two free parameters only and give a good fit.

The mass dependence of the volume integrals shows a clear dependence on the radii of the scattering nuclei, not on the mass number, as obtained in several studies for nucleon scattering with intermediate and heavy nuclei. Also, the imaginary volume integrals of the OP for the proton-halo nuclei scattering have the largest values in comparison with their isotopes.

Generally, the microscopic OP that was used in this work has only a few limited fitting parameters. The renormalization factors showed clear systematic behaviors with respect to the incident energy and strong dependencies on the rms radii. Hence, it is possible to predict a realistic strength of the real and imaginary part of the proton-nucleus potential for systems without needing to use the fitting procedure. Therefore, more experimental data for exotic nuclei with a whole angular range are needed to give accurate parameters of the parametrizations.

[1] P. E. Hodgson, Rep. Prog. Phys. **34**, 765 (1971).
[2] D. Garreta, J. Sura, and A. Tarrats, Nucl. Phys. A **132**, 204 (1969).
[3] S. M. Bunch, H. H. Forster, and C. C. Kim, Nucl. Phys. **53**, 241 (1964).
[4] M. K. Brussel and J. H. Williams, Phys. Rev. **106**, 286 (1957).
[5] K. Imai *et al*., Nucl. Phys. A **325**, 397 (1979).
[6] S. Burzynski, J. Campbell, M. Hammans, R. Henneck, W. Lorenzon, M. A. Pickar, and I. Sick, Phys. Rev. C **39**, 56 (1989).
[7] L. G. Votta, P. G. Roos, N. S. Chant, and R. Woody, III, Phys. Rev. C **10**, 520 (1974).
[8] V. Comparat *et al*., Phys. Rev. C **12**, 251 (1975).
[9] R. Wolski *et al*., Phys. Lett. B **467**, 8 (1999).
[10] S. V. Stepantsov *et al*., Phys. Lett. B **542**, 35 (2002).
[11] L. Giot *et al*., Phys. Rev. C **71**, 064311 (2005).
[12] V. Lapoux *et al*., Phys. Lett. B **517**, 18 (2001).
[13] A. Lagoyannis *et al*., Phys. Lett. B **518**, 27 (2001).
[14] M. D. Cortina-Gil *et al*., Phys. Lett. B **371**, 14 (1996).
[15] M. D. Cortina-Gil *et al*., Nucl. Phys. A **616**, 215c (1997).
[16] A. A. Korsheninnikov *et al*., Nucl. Phys. A **616**, 189c (1997).
[17] A. A. Korsheninnikov *et al*., Nucl. Phys. A **617**, 45 (1997).
[18] M. Hatano *et al*., Eur. J. Phys. A **25**, 255 (2005).
[19] T. Uesaka *et al*., Phys. Rev. C **82**, 021602(R) (2010).
[20] S. Sakaguchi *et al*., Phys. Rev. C **84**, 024604 (2011).
[21] F. Skaza *et al*., Phys. Rev. C **73**, 044301 (2006).
[22] R. Wolski *et al*., Nucl. Phys. A **701**, 29c (2002).
[23] A. A. Korsheninnikov *et al*., Phys. Lett. B **343**, 53 (1995).
[24] A. A. Korsheninnikov *et al*., Phys. Lett. B **316**, 38 (1993).
[25] M. Haller, M. Betz, W. Kretschmer, A. Rauscher, R. Schmitt, and W. Schuster, Nucl. Phys. A **496**, 189 (1989).
[26] K. H. Bray *et al*., Nucl. Phys. A **189**, 35 (1972).
[27] G. S. Mani, D. Jacques, and A. D. B. Dix, Nucl. Phys. A **165**, 145 (1971).
[28] P. J. Dortmans, K. Amos, S. Karataglidis, and S. Raynal, Phys. Rev. C **58**, 2249 (1998).
[29] R. Henneck *et al*., Nucl. Phys. A **571**, 541 (1994).
[30] R. S. Henderson *et al*., Nucl. Phys. A **372**, 117 (1981).
[31] B. Geoffrion, N. Marty, M. Morlet, B. Tatischeff, and A. Willis, Nucl. Phys. A **116**, 209 (1968).
[32] K. Kilian, G. Clausnitzer, W. Dürr, D. Fick, R. Fleischmann, and H. M. Hofmann, Nucl. Phys. A **126**, 529 (1969).
[33] F. Petrovich, R. H. Howell, C. H. Poppe, S. M. Austin, and G. M. Crawley, Nucl. Phys. A **383**, 355 (1982).
[34] C. B. Moon *et al*., Phys. Lett. B **297**, 39 (1992).
[35] A. A. Korsheninnikov *et al*., Phys. Rev. Lett. **78**, 2317 (1997).
[36] A. A. Korsheninnikov *et al*., Phys. Rev. C **53**, R537 (1996).
[37] D. Gupta, C. Samanta, and R. Kanungo, Nucl. Phys. A **674**, 77 (2000).
[38] K. V. Lukyanov, V. K. Lukyanov, E. V. Zemlyanaya, A. N. Antonov, and M. K. Gaidarov, Eur. J. Phys. A **33**, 389 (2007).
[39] V. K. Lukyanov, E. V. Zemlyanaya, K. V. Lukyanov, D. N. Kadrev, A. N. Antonov, M. K. Gaidarov, and S. E. Massen, Phys. Rev. C **80**, 024609 (2009).
[40] Syed Rafi, A. Bhagwat, W. Haider, and Y. K. Gambhir, Phys. Rev. C **86**, 034612 (2012).
[41] Hairui Guo, Yukinobu Watanabe, Takuma Matsumoto, Kazuyuki Ogata, and Masanobu Yahiro, Phys. Rev. C **87**, 024610 (2013).
[42] J. P. Jeukenne, A. Lejeune, and C. Mahaux, Phys. Rev. C **16**, 80 (1977).
[43] M. Y. H. Farag, E. H. Esmael, and H. M. Maridi, Eur. J. Phys. A **48**, 154 (2012).
[44] G. R. Satchler and W. G. Love, Phys. Rep. **55**, 183 (1979).
[45] G. F. Bertsch, J. Borysowicz, H. Mcmanus, and W. G. Love, Nucl. Phys. A **284**, 399 (1977).
[46] V. K. Lukyanov, E. V. Zemlyanaya, and K. V. Lukyanov, Phys. At. Nucl. **69**, 240 (2006).
[47] P. Shukla, arXiv:nucl-th/0112039 (2001).
[48] S. K. Charagi and S. K. Gupta, Phys. Rev. C **41**, 1610 (1990).
[49] I. Tanihata, D. Hirata, T. Kobayashi, S. Shimoura, K. Sugimoto, and H. Toki, Phys. Lett. B **289**, 261 (1992).
[50] G. F. Bertsch and H. Esbensen, Ann. Phys. **209**, 327 (1991).
[51] G. F. Bertsch, B. A. Brown, and H. Sagawa, Phys. Rev. C **39**, 1154 (1989).
[52] M. V. Zhukov, B. V. Danilin, D. V. Fedorov, J. M. Bang, I. J. Thompson, and J. S. Vaagen, Phys. Rep. **231**, 151 (1993).
[53] M. V. Zhukov, A. A. Korsheninnikov, and M. H. Smedberg, Phys. Rev. C **50**, 1(R) (1994).
[54] S. Karataglidis, B. A. Brown, K. Amos, and P. J. Dortmans, Phys. Rev. C **55**, 2826 (1997).
[55] S. Karataglidis, P. J. Dortmans, K. Amos, and C. Bennhold, Phys. Rev. C **61**, 024319 (2000).
[56] G. D. Alkhazov *et al*., Phys. Rev. Lett. **78**, 2313 (1997).
[57] G. D. Alkhazov *et al*., Nucl. Phys. A **712**, 269 (2002).
[58] G. D. Alkhazov, A. V. Dobrovolsky, and A. A. Lobodenko, Nucl. Phys. A **734**, 361 (2004).
[59] S. R. Neumaier *et al*., Nucl. Phys. A **712**, 247 (2002).
[60] P. Egelhof, Prog. Part. Nucl. Phys. **46**, 307 (2001).
[61] P. Egelhof *et al*., Eur. Phys. J. A **15**, 27 (2002).
[62] P. Egelhof, Nucl. Phys. A **722**, 254 (2003).
[63] A. V. Dobrovolsky *et al*., Nucl. Phys. A **766**, 1 (2006).
[64] M. P. Bush, J. S. Al-Khalili, J. A. Tostevin, and R. C. Johnson, Phys. Rev. C **53**, 3009 (1996).
[65] Steven C. Pieper, K. Varga, and R. B. Wiringa, Phys. Rev. C **66**, 044310 (2002).
[66] Steven C. Pieper and R. B. Wiringa, Ann. Rev. Nucl. Part. Sci. **51**, 53 (2001).
[67] R. B. Wiringa, Steven C. Pieper, J. Carlson, and V. R. Pandharipande, Phys. Rev. C **62**, 014001 (2000).
[68] I. Brida, Steven C. Pieper, and R. B. Wiringa, Phys. Rev. C **84**, 024319 (2011).
[69] R. L. Varner, W. J. Thompson, T. L. McAbee, E. J. Ludwig, and T. B. Clegg, Phys. Rep. **201**, 57 (1991).
[70] M. Y. M. Hassan, M. Y. H. Farag, E. H. Esmael, and H. M. Maridi, Phys. Rev. C **79**, 014612 (2009).
[71] V. K. Lukyanov, D. N. Kadrev, E. V. Zemlyanaya, A. N. Antonov, K. V. Lukyanov, and M. K. Gaidarov, Phys. Rev. C **82**, 024604 (2010).
[72] A. de Vismes *et al*., Nucl. Phys. A **706**, 295 (2002).
[73] A. M. Sourkes, A. Houdayer, W. T. H. van Oers, R. F. Carlson, and R. E. Brown, Phys. Rev. C **13**, 451 (1976).
[74] R. F. Carlson *et al*., Nucl. Phys. A **445**, 57 (1985).
[75] A. de Vismes *et al*., Phys. Lett. B **505**, 15 (2001).
[76] I. Tanihata *et al*., Phys. Lett. B **206**, 592 (1988).
[77] P. Mohr, Phys. Rev. C **61**, 045802 (2000).
[78] O. V. Bespalova, E. A. Romanovsky, and T. I. Spasskaya, J. Phys. G: Nucl. Part. Phys. **29**, 1193 (2003).
[79] A. J. Koning and J. P. Delaroche, Nucl. Phys. A **713**, 231 (2003).
[80] Xiaohua Li and Chonghai Cai, Nucl. Phys. A **801**, 43 (2008).
[81] G. E. Brown and M. Rho, Nucl. Phys. A **372**, 397 (1981).
[82] J. P. Jeukenne and C. Mahaux, Nucl. Phys. A **394**, 445 (1983).

[83] E. Somorjai *et al*., Astron. Astrophys. **333**, 1112 (1998).
[84] P. Demetriou, C. Grama, and S. Goriely, Nucl. Phys. A **707**, 253 (2002).
[85] Zs. Fülöp *et al*., Phys. Rev. C **64**, 065805 (2001).
[86] A. Nadasen, S. Balaji, J. Brace, K. A. G. Rao, P. G. Roos, P. Schwandt, and J. T. Ndefru, Phys. Rev. C **66**, 064605 (2002).
[87] U. Atzrott, P. Mohr, H. Abele, C. Hillenmayer, and G. Staudt, Phys. Rev. C **53**, 1336 (1996).
[88] G. Audi, A. H. Wapstra, and C. Thibault, Nucl. Phys. A **729**, 337 (2003).
[89] E. A. Romanovsky *et al*., Bull. Russ. Acad. Sci. Phys. **62**, 150 (1998).
[90] W. T. H. Van Oers and H. Haw, Phys. Lett. B **45**, 227 (1973).
[91] M. E. Brandan and G. R. Satchler, Phys. Rep. **285**, 143 (1997).
[92] G. D. Alkhazov, Yu. Shabelski, and I. S. Novikov, Int. J. Mod. Phys. E **20**, 583 (2011).
[93] I. Tanihata *et al*., Phys. Rev. Lett. **55**, 2676 (1985).
[94] P. Mueller *et al*., Phys. Rev. Lett. **99**, 252501 (2007).
[95] R. Sánchez *et al*., Phys. Rev. Lett. **96**, 033002 (2006).
[96] R. Kanungo and C. Samanta, Nucl. Phys. A **617**, 265 (1997).
[97] M. Avrigeanu, G. S. Anagnostatos, A. N. Antonov, and V. Avrigeanu, Int. J. Mod. Phys. E **11**, 249 (2002).